EES Batteries

ROYAL SOCIETY OF CHEMISTRY

PAPER

View Article Online
View Journal | View Issue

Cite this: *EES Batteries*, 2025, **1**, 867

Hybrid superlattice cathodes unlocking diffusion-barrier-free proton storage for high-rate Zn–MnO_2 batteries†

Yumin Chen,[a] Da Zhang,[a] Chengmin Hu,[c] Pingxuan Liu,[a] Xiaozhe Yang,[a] Hui Duan,[a] Ling Miao,[a] Yaokang Lv,[d] Ziyang Song,*[a] Lihua Gan *[a,b] and Mingxian Liu *[a,b]

Received 5th February 2025,
Accepted 19th May 2025

DOI: 10.1039/d5eb00022j

rsc.li/EESBatteries

Diffusion-controlled Zn^{2+} intercalation often suffers from strong lattice repulsion when using a MnO_2 cathode in Zn-ion batteries, leading to slow reaction kinetics and irreversible phase transitions. Boosting intercalation-barrier-free Grotthuss proton storage in competition with Zn^{2+} in the MnO_2 host provides a highly promising path to develop high-kinetics and stable Zn-ion batteries, but this remains challenging. Here we incorporate tetraamino-benzoquinone (TABQ) into a nickel-doped δ-MnO_2 host to design a two-dimensional hybrid superlattice cathode (Ni–TABQ@δ-MnO_2), which triggers ultrafast proton transfer *via* Grotthuss topochemistry. Conductive Ni–TABQ effectively modulates the electronic properties of δ-MnO_2 through π–d electron coupling, enabling a transition from semiconducting to metallic behavior and markedly increasing the current response from 205 to 305 pA. Furthermore, the intermolecular H-bonding network between the coordination water of Ni–TABQ and lattice oxygen of δ-MnO_2 allows H_3O^+ to transfer protons through the continuous breaking and reformation of O–H bonds. Accordingly, dynamic proton hopping within the Ni–TABQ@δ-MnO_2 cathode shows an ultralow energy barrier (0.124 eV) compared to Zn^{2+} intercalation (0.741 eV), leading to superior rate capacities (453 mA h g^{-1} at 0.2 A g^{-1}; 151 mA h g^{-1} at 10 A g^{-1}) and a long lifespan (8000 cycles). This study gives new insights into the design of diffusion-barrier-free proton-conductive hybrid superlattice cathodes for advanced energy storage.

Broader context

Aqueous rechargeable Zn–MnO_2 batteries have gained significant attention due to their inherent safety, low cost and favorable operating voltages, making them promising candidates for large-scale energy storage. However, the large size and high desolvation energy of $[Zn(H_2O)_6]^{2+}$ ions result in sluggish intercalation kinetics and diminished (dis)charge rates in Zn–MnO_2 batteries. Additionally, the strong lattice repulsion between Zn^{2+} ions and the MnO_2 host often leads to irreversible phase transitions and structural collapse, severely compromising the rate capacity and cycling stability. In this work, we design a hybrid superlattice cathode (Ni–TABQ@δ-MnO_2), which triggers ultrafast proton transfer *via* Grotthuss topochemistry. Conductive Ni–TABQ effectively modulates the electronic properties of δ-MnO_2 through π–d electron coupling, and the intermolecular H-bonds between coordination water (Ni–TABQ) and lattice oxygen (δ-MnO_2) facilitate dynamic proton transfer through the continuous breaking and reformation of the H-bonding network. The unique proton hopping processes empower Zn–MnO_2 to deliver a high-rate and ultrastable charge storage process. This study may shed new light on the design of diffusion-barrier-free proton-conductive hybrid superlattice cathodes for advanced energy storage.

Introduction

Aqueous rechargeable zinc-ion batteries (ZIBs) have gained significant attention due to their inherent safety, low cost, and the high theoretical capacity of zinc anodes (820 mA h g^{-1}) coupled with a favorable redox potential (−0.76 V *vs.* standard hydrogen electrode), making ZIBs promising candidates to act as large-scale energy storage solutions.[1–5] Among the various Zn^{2+}-hosting inorganic cathode materials, manganese-based oxides show significant properties, such as a high theoretical capacity, favorable operating voltage and natural abundance.[6–10] In particular, layered δ-MnO_2 has a two-dimensional open crystal structure and large interlayer

[a]*Shanghai Key Lab of Chemical Assessment and Sustainability, School of Chemical Science and Engineering, Tongji University, 1239 Siping Rd., Shanghai, 200092, P. R. China. E-mail: 21310240@tongji.edu.cn, ganlh@tongji.edu.cn, liumx@tongji.edu.cn*

[b]*State Key Laboratory of Cardiovascular Diseases and Medical Innovation Center, Shanghai East Hospital, School of Medicine, Tongji University, 150 Jimo Rd., Shanghai 200120, P. R. China*

[c]*Department of Chemistry, State Key Laboratory of Molecular Engineering of Polymers, Shanghai Key Laboratory of Molecular Catalysis and Innovative Materials, Fudan University, 220 Handan Rd., Shanghai 200433, P. R. China*

[d]*College of Chemical Engineering, Zhejiang University of Technology, Hangzhou 310014, P. R. China*

† Electronic supplementary information (ESI) available. See DOI: https://doi.org/10.1039/d5eb00022j

spacing enabling efficient charge-carrier (de)intercalation, distinguishing it among manganese-based oxides and making it an ideal candidate for high-performance energy storage.[11–15] However, the large hydrated structure and high desolvation energy of $[Zn(H_2O)_6]^{2+}$ ions pose significant challenges, triggering sluggish intercalation kinetics and (dis)charge rates in ZIBs.[16–18] Additionally, strong lattice repulsion between Zn^{2+} ions and the δ-MnO_2 host lattice often triggers irreversible phase transitions and structural collapse, further limiting the capacity performance and cycling stability.[19–22] Addressing these issues requires innovative approaches to optimize the charge storage behavior of manganese-based cathodes and stabilize their structures during cycling.

Compared with sluggish Zn^{2+} storage, protons (H^+), having the smallest size and lightest weight, can enable fast (de)intercalation kinetics and reduce structural degradation in Mn-based hosts during cycling, significantly improving the rate performance and high-power energy storage of ZIBs.[23–26] Therefore, activating superior H^+ storage offers a compelling solution to overcome the electrochemical limitations of Zn^{2+}, with significant potential to improve the rate performance and lifespan of Zn–MnO_2 batteries.[27–30] For instance, Pan *et al.* introduced the Grotthuss proton transport mechanism in α-MnO_2, highlighting the rapid proton migration within the [2 × 2]-tunnel structure.[31] He *et al.* showed that the lattice water in $NiMn_3O_7{\cdot}3H_2O$ facilitates hydrated proton migration to interlayer spaces, where protons bind with O^{2-} ions in the Mn–O layer, thereby enabling efficient charge transport and structural stability during cycling.[32] These findings highlight the critical role of the crystal structure in facilitating proton migration and enhancing electrochemical performance. However, during prolonged cycling, competition with Zn^{2+} insertion and the structural instability of reported Mn-based host materials frequently undermine the efficiency of Zn–MnO_2 energy storage systems, leading to decreased proton storage, especially at high current densities. Therefore, it is of great significance to precisely design Mn-based cathodes with more favorable crystal lattice structures for better selective proton intercalation for the purpose of propelling high-performance Zn–MnO_2 batteries.

In this work, a hybrid superlattice Ni–TABQ@δ-MnO_2 cathode is designed to enhance proton transfer by taking advantage of the Grotthuss topochemistry mechanism. Incorporated conductive Ni–TABQ can modulate the electronic properties of δ-MnO_2 *via* π–d electron coupling, establishing efficient conductive pathways. Moreover, rich intermolecular H-bonds between coordination water (Ni–TABQ) and lattice oxygen (δ-MnO_2) facilitate proton conduction for rapid redox reactions, and the formed intermolecular H-bonding network allows H_3O^+ to transfer protons through the continuous breaking and reformation of O–H bonds. This dynamic hopping of protons significantly reduces the charge-transfer energy barrier compared to the (de)intercalation of Zn^{2+} (0.082 eV *vs.* 0.741 eV), enabling fast and stable energy storage. As a result, the Ni–TABQ@δ-MnO_2 cathode demonstrates excellent performance, including high capacity, large-current tolerance, and an ultralong lifespan. This study paves the way for the development of Grotthuss proton-conductive hybrid superlattice cathodes towards advanced energy storage.

Results and discussion

During the cyclic charging and discharging of a layered δ-MnO_2 cathode, zinc-ion insertion induces strong lattice repulsion and irreversible phase transitions, resulting in rapid structural degradation and performance decline. A widely adopted approach to mitigate these effects is cation pillar engineering.[24,33] While cation pre-intercalation modestly enhances the (de)intercalation kinetics of Ni–δ-MnO_2, it leads to limited improvement of its intrinsic electronic properties. Additionally, cation pillar dissolution during ion exchange over periods of extended cycling compromises structural integrity, leading to a sharp decline in capacity retention (Fig. S1†). To address these challenges, TABQ was selected due to its conjugated planar structure and easy combination with Ni^{2+} ions to form a π–d electronic coupling configuration; these are beneficial for boosting electronic conductivity and triggering ultrafast proton transfer *via* Grotthuss topochemistry, thereby optimizing the electrochemical properties. We innovatively incorporate TABQ into Ni–δ-MnO_2 to form a two-dimensional conductive metal–organic framework (Ni–TABQ). This framework further integrates with the δ-MnO_2 host to construct an organic–inorganic hybrid superlattice structure (Ni–TABQ@δ-MnO_2). The hybrid superlattice cathode combines the superior electronic conductivity of the organic components with the high-energy storage capabilities of the δ-MnO_2 lattice, offering a promising solution for zinc-ion energy storage. Furthermore, the superlattice architecture enables precise control over the lattice arrangement and interfaces of the organic and inorganic components, significantly enhancing the proton transfer efficiency. This synergistic integration optimizes the electronic properties and rate performance of the Ni–TABQ@δ-MnO_2 cathode, making it a robust candidate for use in high-rate and stable energy storage systems (Fig. 1a).

Rietveld refinement of the crystal diffraction profiles (Fig. 1b) shows that the hybrid superlattice Ni–TABQ@δ-MnO_2 cathode retains the same monoclinic phase (*C*2/*m* space group) as δ-MnO_2, with refined lattice parameters of $\alpha = \gamma = 90°$, $\beta = 116.99°$, $a = 10.38$, $b = 5.84$, and $c = 8.09$ Å, achieving a satisfactory agreement factor (R_{wp} = 6.47%). Morphological characterization shows that δ-MnO_2, Ni–δ-MnO_2 and Ni–TABQ all feature nanoflower structures composed of nanosheets (Fig. S2a–f and S3†). Notably, Ni–TABQ@δ-MnO_2 retains its morphology after incorporating the TABQ component into the Ni–δ-MnO_2 framework (Fig. 1c and Fig. S2g–i†), which is helpful for the exposure of active sites and fast ion (de)intercalation. Fourier transform infrared (FT-IR) spectra (Fig. 1d) and thermogravimetric analysis results (Fig. S4†) further confirm that TABQ has been successfully incorporated into the Ni–δ-MnO_2 host.[34] High-resolution transmission electron

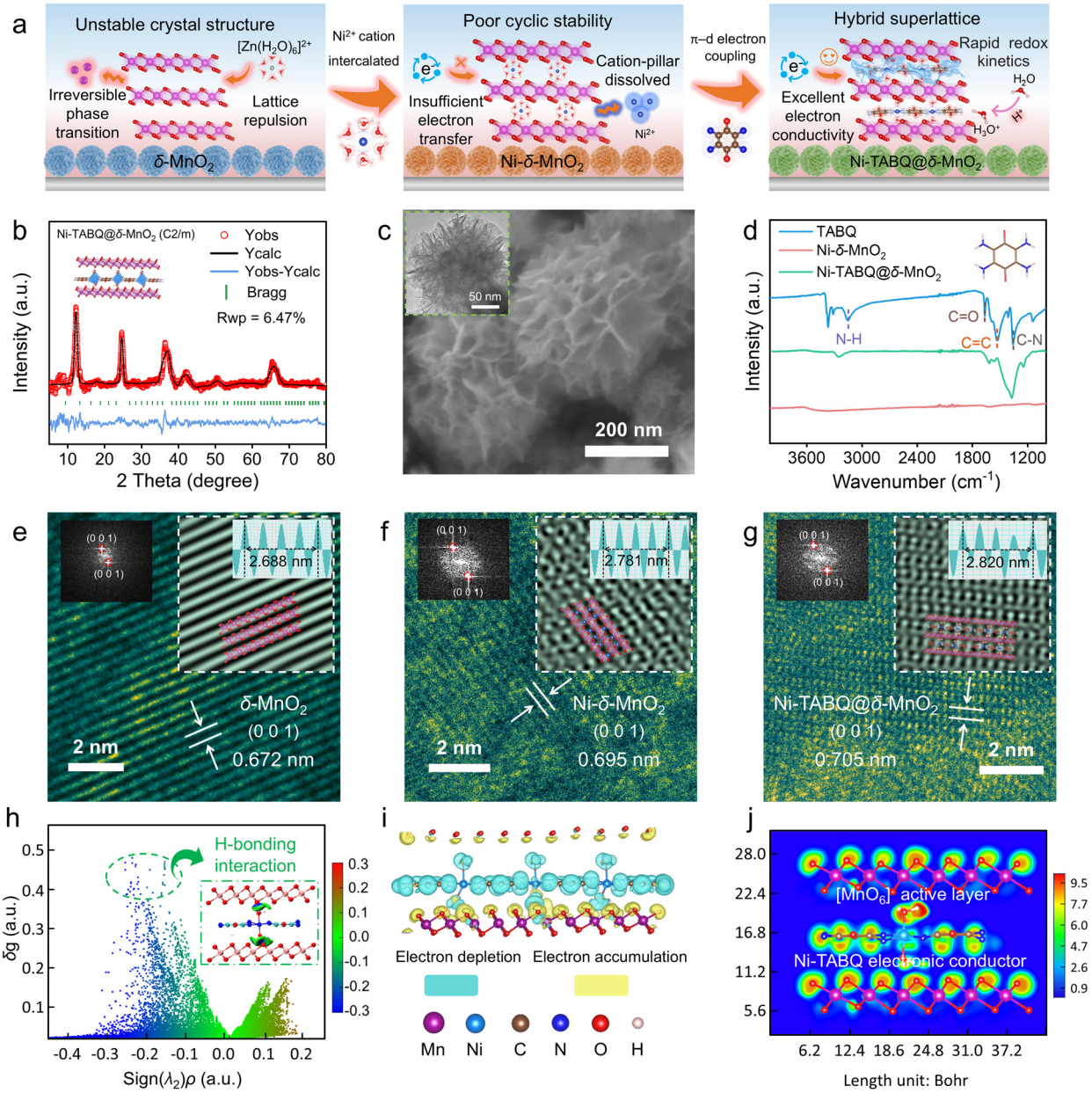

Fig. 1 (a) A schematic diagram of the three energy storage mechanisms at the cathode interface. (b) Rietveld-refined crystal diffraction profiles of Ni–TABQ@δ-MnO_2. (c) SEM and TEM (inset) images of Ni–TABQ@δ-MnO_2. (d) FT-IR spectra. HRTEM images of (e) δ-MnO_2, (f) Ni–δ-MnO_2, and (g) Ni–TABQ@δ-MnO_2 (inset: inverse fast Fourier transform). Structural and electronic property analysis of Ni–TABQ@δ-MnO_2: (h) IGM scatter plots, (i) differential electron density isosurfaces, and (j) an ELF map of the optimized crystal structure.

microscopy (HRTEM) images provide detailed insights into the crystal structure and diffraction planes of manganese-based materials. For δ-MnO_2, a monoclinic crystal structure with an interlayer spacing of 0.672 nm along the (100) plane is observed, which expands to 0.695 nm upon pre-intercalation with Ni^{2+} cation pillars (Fig. 1e and f). Further characterization of Ni–TABQ@δ-MnO_2 based on HRTEM and fast Fourier transformation (FFT) patterns (Fig. 1g) confirms the successful incorporation of TABQ into the (001) plane of Ni–δ-MnO_2. The integration of Ni–TABQ induces the formation of a hybrid superlattice structure, further expanding the interlayer spacing to 0.705 nm. XRD patterns substantiate these changes, showing broadened (001) peaks and their shift to lower 2θ angles (Fig. S5†), indicative of improved crystallinity and interlayer expansion.[35] HRTEM maps reveal the distinct elemental signals of Ni and N, originating from Ni–TABQ, further confirming the uniform integration of TABQ into the Ni–δ-MnO_2 crystal framework to form the hybrid superlattice Ni–TABQ@δ-MnO_2 cathode (Fig. S6†).

Density functional theory (DFT) simulations were conducted to investigate the intermolecular forces and electronic properties of Ni–TABQ@δ-MnO_2. The independent gradient

model based on Hirshfeld partitioning (IGM), analyzed as a function of electron density, reveals the robust hydrogen bonding interactions (H···O) between the coordination water molecules in Ni–TABQ and the lattice oxygen in δ-MnO_2 (Fig. 1h).[36–38] These strong interactions establish high-speed channels for proton transfer across the interlayers, significantly enhancing the ion transport efficiency. Differential electron density isosurfaces demonstrate charge transfer from Ni–TABQ to the lattice oxygen of δ-MnO_2, further confirming that interlayer H-bonds facilitate electron transfer during electrochemical redox processes (Fig. 1i and Fig. S7†). Electron localization function (ELF) maps provide additional insights into the bonding characteristics of the hybrid superlattice, showing pronounced electron localization around the coordination water molecules, highlighting strong H-bonding interactions (Fig. 1j).[39,40] Overall, the hybrid superlattice structure strengthens H-bonding and the electronic properties of Ni–TABQ@δ-MnO_2, underlining the synergistic effect of Ni–TABQ on the structural and electrochemical properties of δ-MnO_2.

Band structure and density of state calculations were performed to elucidate the electronic properties of δ-MnO_2 and Ni–TABQ@δ-MnO_2 (Fig. S8†). The layered δ-MnO_2 crystal structure restricts electron conduction, resulting in a wide bandgap (0.955 eV) and semiconductor-like behavior (Fig. 2a and

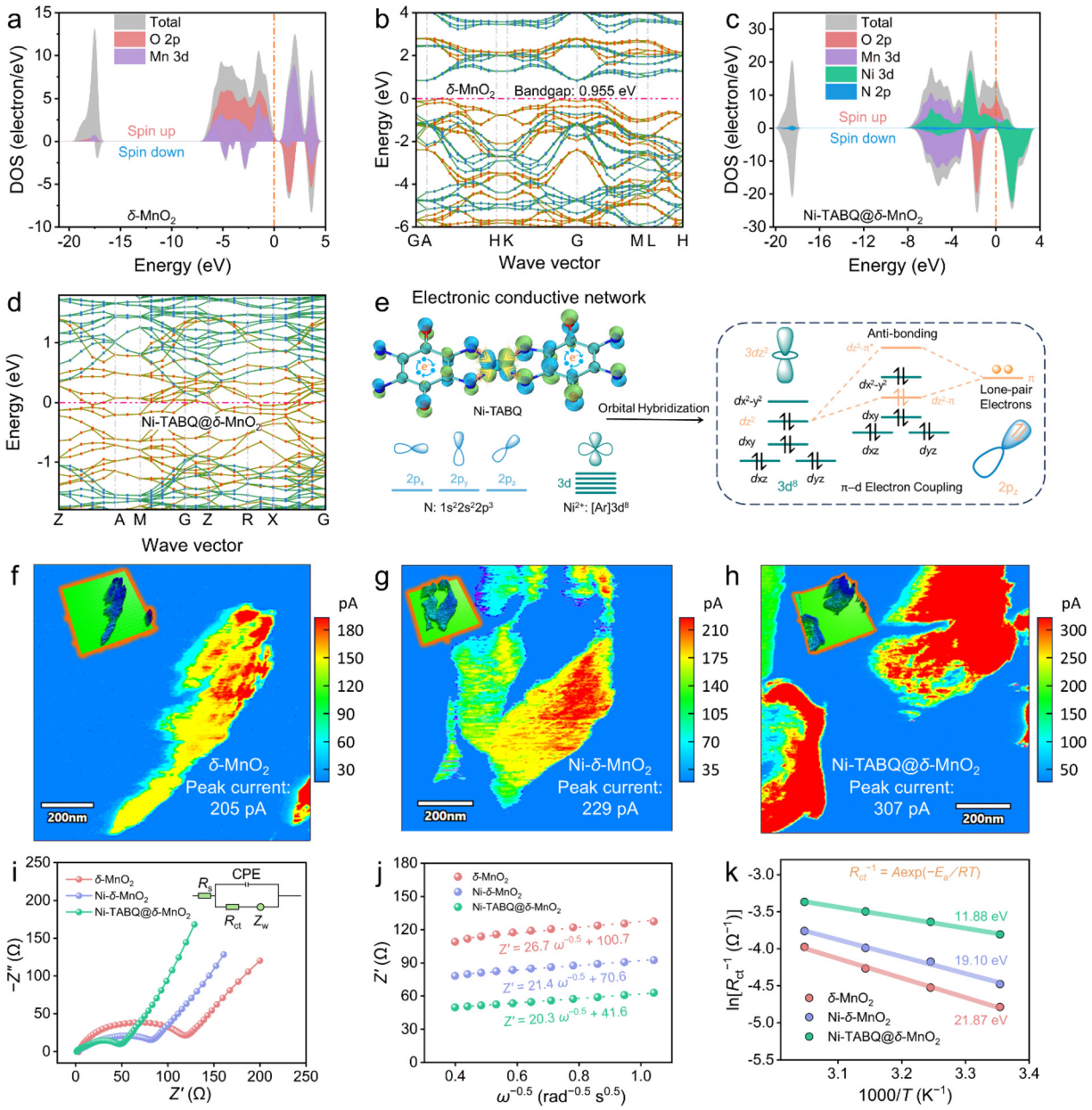

Fig. 2 Electronic structure and orbital analysis. The density of states and band structure of (a and b) δ-MnO_2 and (c and d) Ni–TABQ@δ-MnO_2. (e) Orbital hybridization of conductive Ni–TABQ MOFs. Conductive atomic force microscopy mapping images of (f) δ-MnO_2, (g) Ni–TABQ@δ-MnO_2 and (h) Ni–TABQ@δ-MnO_2. Electrochemical property analysis. (i) EIS spectra. (j) The relationship between Z' and $\omega^{-0.5}$. (k) E_a values.

b).[41,42] After introducing Ni–TABQ MOFs as interlayer electron carriers, metallic properties emerge, markedly enhancing the conductivity (Fig. 2c and d). Through the hybridization of Ni-3d and N-2p orbitals, Ni–TABQ MOFs enable π–d electron coupling to establish an electronic conductive network that facilitates both ion and electron transfer (Fig. 2e).[43,44] Conductive atomic force microscopy (CAFM) was employed to evaluate the local current distribution on the surface of manganese-based materials, providing precise insights into their conductivity behavior (Fig. S9†). As depicted in Fig. 2f, δ-MnO_2 demonstrates a peak current of 205 pA, accompanied by an uneven current distribution, indicating its limited intrinsic conductivity. Upon doping with Ni^{2+} cation pillars, the peak current slightly increases to 229 pA, reflecting a moderate improvement in conductivity (Fig. 2g). In contrast, the most significant enhancement of peak current (307 pA) is observed in Ni–TABQ@δ-MnO_2 (Fig. 2h). This improvement is accompanied by a notably uniform current distribution across the surface, highlighting the superior electronic transport pathways established by the conductive Ni–TABQ. The enhanced conductivity can be attributed to the π–d electron coupling induced electron transfer in the hybrid superlattice structure, which collectively facilitated faster ion and electron mobility.

To evaluate the electrochemical conductivity properties of δ-MnO_2-based cathodes, electrochemical impedance spectroscopy (EIS) analysis was carried out (Fig. 2i and Fig. S10a†). It reveals that the hybrid superlattice Ni–TABQ@δ-MnO_2 cathode achieves a significantly lower charge transfer resistance (R_{ct}) of 48.8 Ω, outperforming both Ni–δ-MnO_2 (88.2 Ω) and δ-MnO_2 (118.5 Ω). The real impedance component Z' and angular frequency ω further verify the superior charge transfer kinetics of the hybrid superlattice structure (Fig. 2j).[45,46] The activation energy (E_a) for charge transfer was obtained using the Arrhenius equation (eqn (S5) and (S6)†). The Ni–TABQ@δ-MnO_2 cathode demonstrates an exceptionally small E_a value of 11.88 kJ mol^{-1} (Fig. 2k and Fig. S10b†), which is significantly lower than those of Ni–δ-MnO_2 (19.10 kJ mol^{-1}) and δ-MnO_2 (21.87 kJ mol^{-1}). These results underscore the high ionic conductivity, efficient ion diffusion pathways, and reduced reaction barrier of the hybrid superlattice structure of Ni–TABQ@δ-MnO_2. The incorporation of Ni–TABQ enhances the charge transfer efficiency and ion transport, highlighting its role in enabling high-kinetics charge storage, and positioning the hybrid superlattice Ni–TABQ@δ-MnO_2 as a promising cathode material for advanced energy storage.

Zn–MnO_2 batteries were constructed, which involve a Zn metal anode, δ-MnO_2-based cathodic materials, and 2 M $ZnSO_4$ + 0.2 M $MnSO_4$ aqueous electrolyte (Fig. S11†). Cyclic voltammetry (CV) curves of Ni–TABQ@δ-MnO_2 (Fig. 3a) exhibit pronounced redox peaks and reduced polarization, indicating its superior redox activity compared to δ-MnO_2 and Ni–δ-MnO_2. The Ni–TABQ@δ-MnO_2 cathode achieves an impressive specific capacity of 453 mA h g^{-1} at 0.2 A g^{-1}, outperforming δ-MnO_2 (236 mA h g^{-1}), Ni–δ-MnO_2 (346 mA h g^{-1}) and Ni–TABQ (12 mA h g^{-1}) (Fig. 3b and Fig. S12†). The Ni–TABQ@δ-MnO_2 cathode also demonstrates excellent rate capacities of 370, 331, 274, 218, 183, and 152 mA h g^{-1} at current densities of 0.5, 0.8, 1, 3, 5, and 10 A g^{-1}, respectively (Fig. 3b and c). Significantly, the Zn‖Ni–TABQ@δ-MnO_2 battery achieves a record energy density of 586 W h kg^{-1} (calculated based on the mass of active cathode material; Fig. 3d and Table S1†), which is superior to reported Mn/V-based and organic cathode materials.[47–54] At mass loadings of 2.9 and 5.0 mg cm^{-2}, the TABQ@δ-MnO_2 cathode delivers capacities of 423 and 362 mA h g^{-1}, respectively. Even at a high mass loading of 10.2 mg cm^{-2}, it retains a remarkable capacity of 289 mA h g^{-1}, highlighting its exceptional large-scale energy storage potential (Fig. S13†). Furthermore, the TABQ@δ-MnO_2 cathode maintains 88.76% of its initial capacity (328 mA h g^{-1}) after 200 cycles at 0.5 A g^{-1}, with high coulombic efficiency (Fig. 3e). Conversely, Ni–δ-MnO_2 and δ-MnO_2 exhibit inferior cycling stability, with low-capacity retention of 45.16% and 34.08% in the absence of the TABQ component, due to the dissolution of pre-intercalated Ni^{2+} cations and structural degradation. Remarkably, even at a high current density of 5 A g^{-1} for 8000 cycles, the capacity retention remains at 93.82%, underscoring the robust structural and electrochemical stability of the hybrid superlattice cathode (Fig. 3e, Fig. S14 and S15†). Three integrated Zn‖Ni–TABQ@δ-MnO_2 batteries can power an LED toy (Fig. S16†), demonstrating the application promise of Zn–MnO_2 batteries.

In addition, the redox kinetics of the Zn‖Ni–TABQ@δ-MnO_2 cell were analyzed by using CV curves and Dunn's method.[55,56] Across scan rates in the range of 0.2–1.0 mV s^{-1}, CV profiles maintain consistent shapes with minor shifts in redox peaks (Fig. S17†), indicating the excellent electrochemical reversibility of the Zn‖Ni–TABQ@δ-MnO_2 battery. Three distinct redox signals (denoted as P_{R1}, P_{R2}, and P_{O1}) are observed, corresponding to the Zn^{2+}/H^+ co-intercalation redox reaction. The power-law relationship between the peak current (i) and scan rate (v) yields b-values of 0.56, 0.77, and 0.53 for the three peaks (Fig. 3g), demonstrating a rapid surface-dominated proton charge storage process coupled with Zn^{2+} intercalation during discharging. Further analysis reveals that the rapid surface capacitive contribution dominates charge storage, accounting for 75.66–94.47% of the total capacity across all scan rates (Fig. 3h and i). However, the b-values and rapid surface capacitive contributions of δ-MnO_2 and Ni–δ-MnO_2 cathodes indicate their slow reaction kinetics processes (Fig. S18 and S19†). These findings underscore the critical role of the conductive Ni–TABQ component in modulating the electronic properties of the hybrid superlattice cathode, facilitating high-power energy storage.

To further identify the charge-storage mechanism of the Ni–TABQ@δ-MnO_2 cathode, spectroscopic characterization was performed to delve into the proton storage behavior in specific potential states (Fig. 4a). Based on *ex situ* XRD patterns (Fig. 4b and Fig. S20†), the peak intensities of $HMnO_2$ at 20.8° and 32.7° increase during discharging (state A → D) and disappear during subsequent charging (state D → G),[32,57] verifying the highly reversible phase transition process. HRTEM

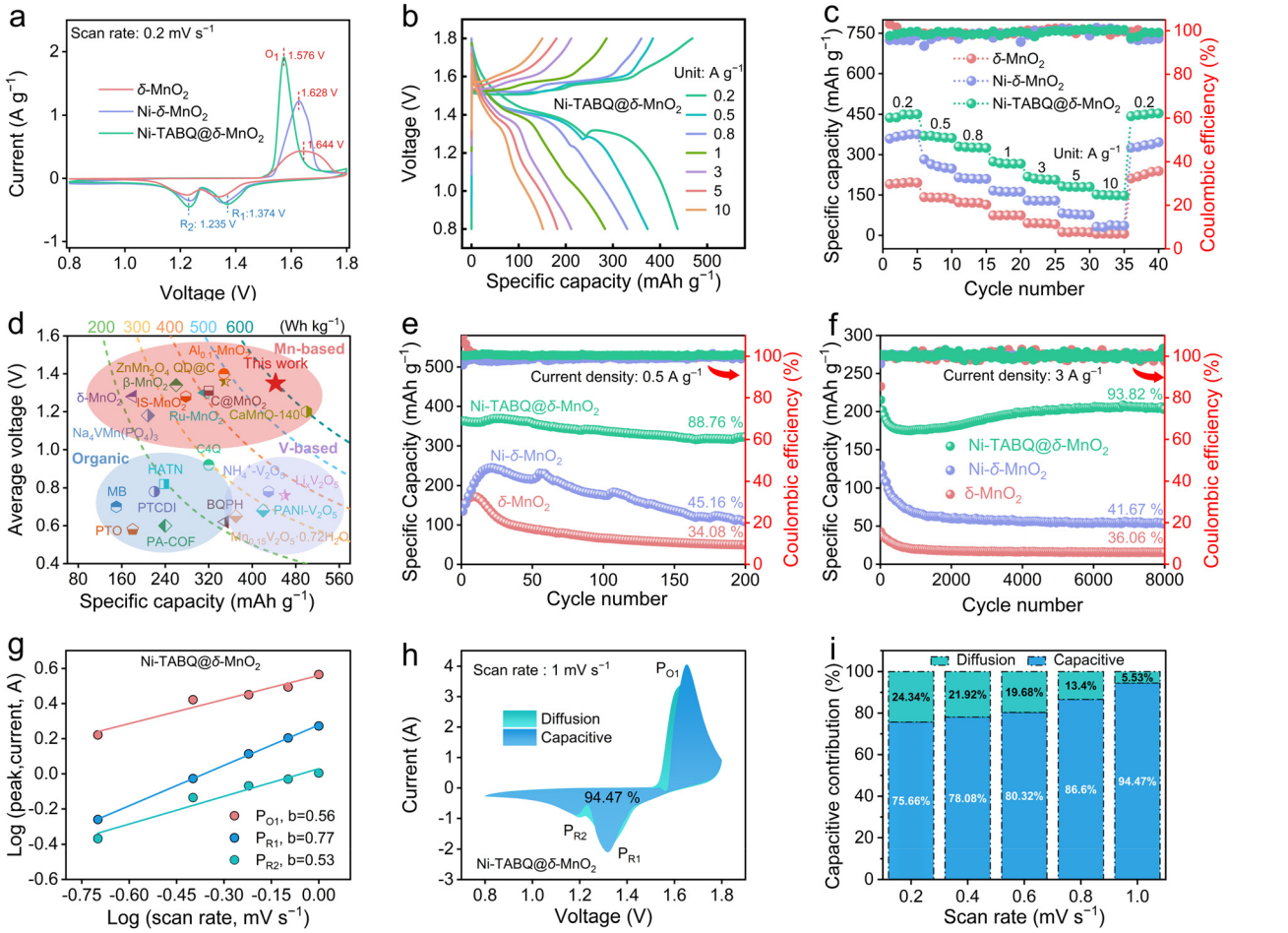

Fig. 3 Electrochemical performances of Zn–MnO_2 batteries. (a) CV curves. (b) GCD profiles. (c) Rate capabilities. (d) Voltage-capacity contour plots of reported Zn batteries. Cycling performance at (e) 0.5 and (f) 3 A g^{-1}. Charge storage kinetics of the Ni–TABQ@δ-MnO_2 hybrid superlattice cathode. (g) Calculated *b* values. (h) Capacitive contribution. (i) Ratios of capacitive and diffusion-controlled contributions at various scan rates.

images in state D further confirm the evolution of $HMnO_2$, accompanied by the appearance of the (1, 1, −1) crystal plane with a width of 0.342 nm (Fig. 4c). Operando pH measurements were conducted to accurately monitor the H^+ redox behavior in the Ni–TABQ@δ-MnO_2 cathode during the discharge/charge process (Fig. S21†). The pH value is significantly boosted from 2.47 to 3.01 during discharging from 1.80–1.25 V. Subsequently, it slightly increases in the voltage range of 1.25–0.80 V, with pH values of 3.01 to 3.09 (Fig. 4d). Such results imply a strong proton-coupled charge storage process in the Ni–TABQ@δ-MnO_2 cathode over the voltage range of 1.80–1.25 V (state A → C). In the subsequent recharging procedure, the pH value returns back to its initial level. In addition, the reversible formation of $Zn_4(OH)_6(SO_4)\cdot 5H_2O$ (ZHS) functions (Fig. S22†) as a pH buffer and holds the solution pH value constant within a certain range.

An electrochemical quartz crystal microbalance (EQCM) was employed for the operando monitoring of the mass change of Ni–TABQ@δ-MnO_2 with continuous ion intercalation. Consistent with the GITT results, the mass change of the Ni–TABQ@δ-MnO_2 electrode during ion intercalation involves two stages. In the first stage (state A → C), the average weight increase calculated based on the curve slope (Fig. 4e) is 19.72 g per mol charge, close to the weight of H_3O^+ (19 g per mol charge), suggesting hydrated proton (H_3O^+) intercalation in Ni–TABQ@δ-MnO_2. Meanwhile, the average weight increase in the second stage (state C → D) is 32.94 g per mol charge, which suggests the intercalation of Zn^{2+} in Ni–TABQ@δ-MnO_2. The galvanostatic intermittent titration technique (GITT) is applied to measure the ion diffusion coefficient (*D*; Fig. 4f and Fig. S23†). The higher *D* values of ~10^{-9} cm^2 s^{-1} during discharging (state A → C) are ascribed to the fast-kinetics incorporation of H^+, while the lower *D* values of ~10^{-11} cm^2 s^{-1} (state C → D) belong to the slow intercalation of Zn^{2+} in the Ni–TABQ@δ-MnO_2 cathode. These results verify the two-step H^+/Zn^{2+} co-intercalation redox process. Thanks to the mixed superlattice structure of Ni–TABQ@δ-MnO_2, protons can be transferred *via* H_2O media through Grotthuss topochemistry, which is beneficial for rapid charge storage and high-power energy storage.

High-resolution X-ray photoelectron spectroscopy (XPS) analysis of the O 1s signal was carried out to elucidate the

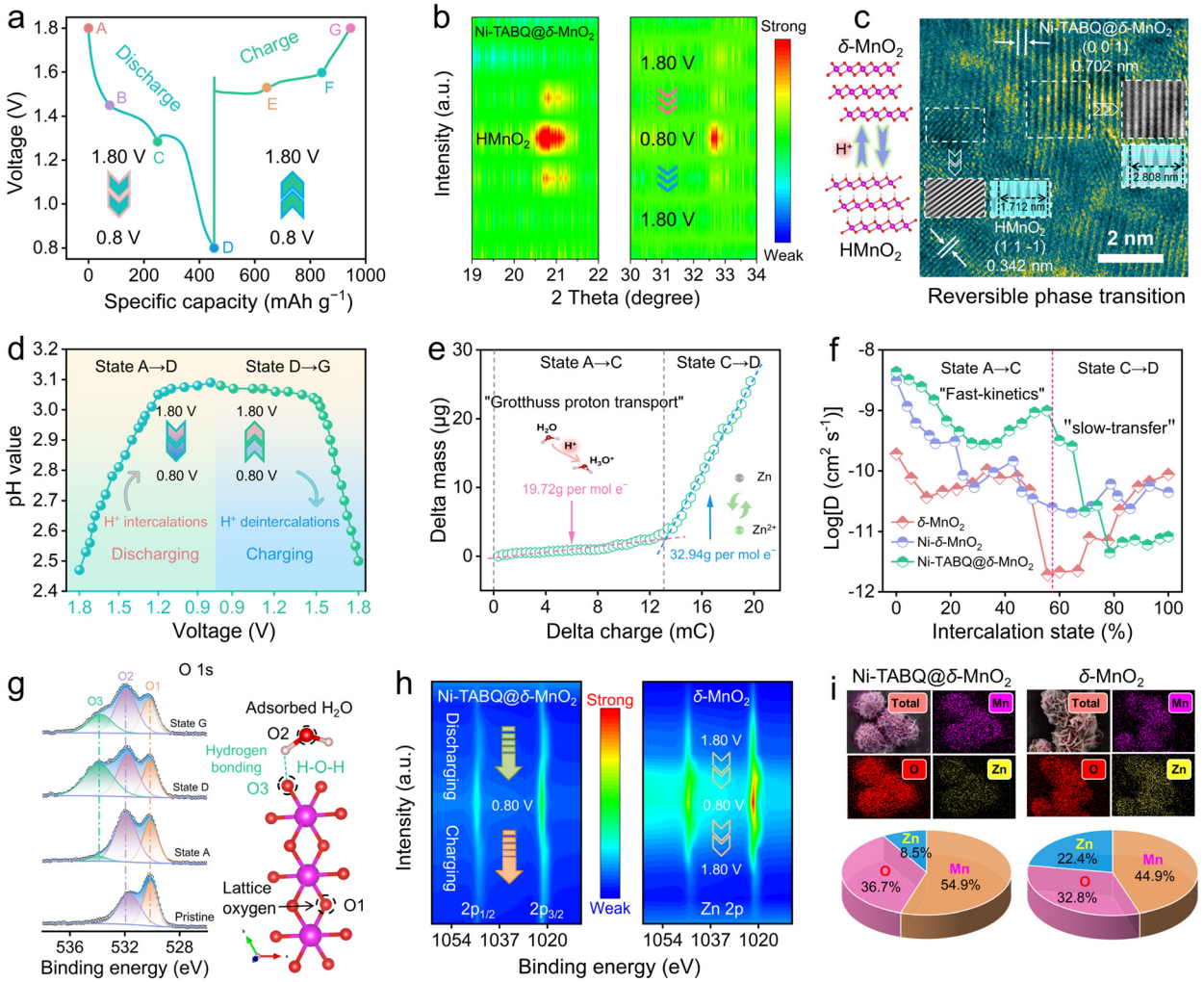

Fig. 4 The Grotthuss proton transfer behavior of the Zn||Ni–TABQ@δ-MnO_2 battery. (a) GCD profiles with selected specific (dis)charge states. (b) *Ex situ* XRD patterns. (c) A HRTEM image of the Ni–TABQ@δ-MnO_2 cathode in the fully discharged state. (d) *In situ* pH variations. (e) The electrode mass change *versus* charge during the discharge (ion-intercalation) process. (f) The ion diffusion coefficient during the discharge process. *Ex situ* (g) O 1s and (h) Zn 2p XPS spectra. (i) Element maps of Ni–TABQ@δ-MnO_2 and δ-MnO_2 cathodes in the fully discharged state.

redox behavior of the Ni–TABQ@δ-MnO_2 cathode during cell operation. In the pristine state, two peaks at 530.1 and 531.7 eV are observed, corresponding to lattice oxygen (O1) and oxygen from adsorbed H_2O (O2), respectively.[58] Notably, an additional peak at 533.8 eV (O3) emerges during the charge/discharge process. This peak is attributed to the terminal oxygens of [MnO_6] bilayers, and it splits from the O2 peak due to H-bond formation with intercalated H_2O/H_3O^+ (as illustrated in Fig. 4g). Compared with Ni–δ-MnO_2 and δ-MnO_2 cathodes, the Mn 2p XPS spectra of Ni–TABQ@δ-MnO_2 reveal the largest fluctuations of Mn valence due to enhanced redox activity from proton involvement (Fig. S24a and b†). This confirms that the extra capacity contribution originates from the multielectron redox activity of Mn sites and is enabled by a strong proton–electron coupling process. The Ni–TABQ@δ-MnO_2 cathode in HOTF–H_2O electrolyte exhibits the highest proton storage capacity of 233.2 mA h g^{-1} (Fig. S24c†), which outperforms Ni–δ-MnO_2 (95.6 mA h g^{-1}) and δ-MnO_2 (52.3 mA h g^{-1}), highlighting the key role of Ni–TABQ incorporation in improving the electrochemical capacity. Operando FT-IR spectra exhibit the generation/disappearance of O–H signals, which derive from reactions between the lattice oxygen of Ni–TABQ@δ-MnO_2 and protons (Fig. S24d†). Such a result confirms the participation of protons through distinct shifts in the O–H stretching bands during the (dis)charge process. Simultaneously, the Zn 2p signal intensity increases during the discharge process (state A → D) due to Zn^{2+} intercalation into the Ni–TABQ@δ-MnO_2 host and weakens during the recharge process (state D → G) as Zn^{2+} ions are extracted (Fig. 4h). Compared to pristine δ-MnO_2, the hybrid superlattice Ni–TABQ@δ-MnO_2 cathode exhibits a reduced Zn^{2+} intercalation capacity due to steric hindrance imposed by Ni–TABQ. Elemental distribution maps of Mn, O, and Zn, along with their relative proportions, further validate the selective ionic storage behavior (Fig. 4i and Fig. S25a and b†). Moreover, coupled plasma optical emission spectroscopy (ICP-OES) ana-

lyses of the Ni–TABQ@δ-MnO_2 cathode at various rates confirmed that proton storage becomes more dominant with increasing current density, reaching 93.91% at 10 A g^{-1} (Fig. S25c and Table S2†). Accordingly, the structural design of hybrid superlattice Ni–TABQ@δ-MnO_2 can not only suppress excessive Zn^{2+} intercalation but also promote efficient proton storage through Grotthuss topochemistry, enabling fast and stable charge storage performance.

To investigate the mechanisms of proton transport and charge storage, DFT calculations were performed to simulate the structural evolution of the Ni–TABQ@δ-MnO_2 cathode during electrochemical reactions. As shown in Fig. 5a, the hybrid superlattice Ni–TABQ@δ-MnO_2 exhibits highly protophilic reactivity (H_3O^+, −1.65 eV) and weaker zincophilic behavior (Zn^{2+}, −0.26 eV), while δ-MnO_2 demonstrates stronger Zn^{2+} adsorption (−1.17 eV) but relatively limited interaction with H_3O^+ (−0.85 eV). The pronounced protophilic activity of Ni–TABQ@δ-MnO_2 facilitates efficient Grotthuss proton conduction. The interaction bonding types were further explored using IGMH and ELF maps. Hydrated protons exhibit strong hydrogen bonding within the hybrid superlattice framework of Ni–TABQ@δ-MnO_2 (Fig. 5b), whereas Zn^{2+} predominantly forms Zn–O ionic bonds (Fig. 5c). In contrast with the rigid Zn–O ionic bonds, the dynamic and flexible nature of H-bonds enhances the proton transport kinetics and charge storage. Differential electron density isosurfaces and Bader charge analysis reveal the charge transfer behavior between charge carriers and the Ni–TABQ@δ-MnO_2 host (Fig. 5d). Notably, H_3O^+ enables better charge transfer to the Ni–TABQ@δ-MnO_2 host (0.824 e) in comparison to Zn^{2+} (0.413 e), further confirming its superior protonophilic reactivity. To evaluate ion diffusion pathways and energy barriers, the climbing-image nudged elastic band (CI-NEB) method was employed. Fig. 5e and Fig. S26† illustrate the migration trajectories of Zn^{2+} and H^+ ions. The calculated activation energy barriers for Zn^{2+} and H^+ migration are 0.741 and 0.124 eV, respectively. The main barrier to Zn^{2+} ion transport in the aqueous electrolyte originates from the spatial steric hindrance imposed by Ni–TABQ layers within the hybrid Ni–TABQ@δ-MnO_2 superlattice structure. In contrast, the hydro-

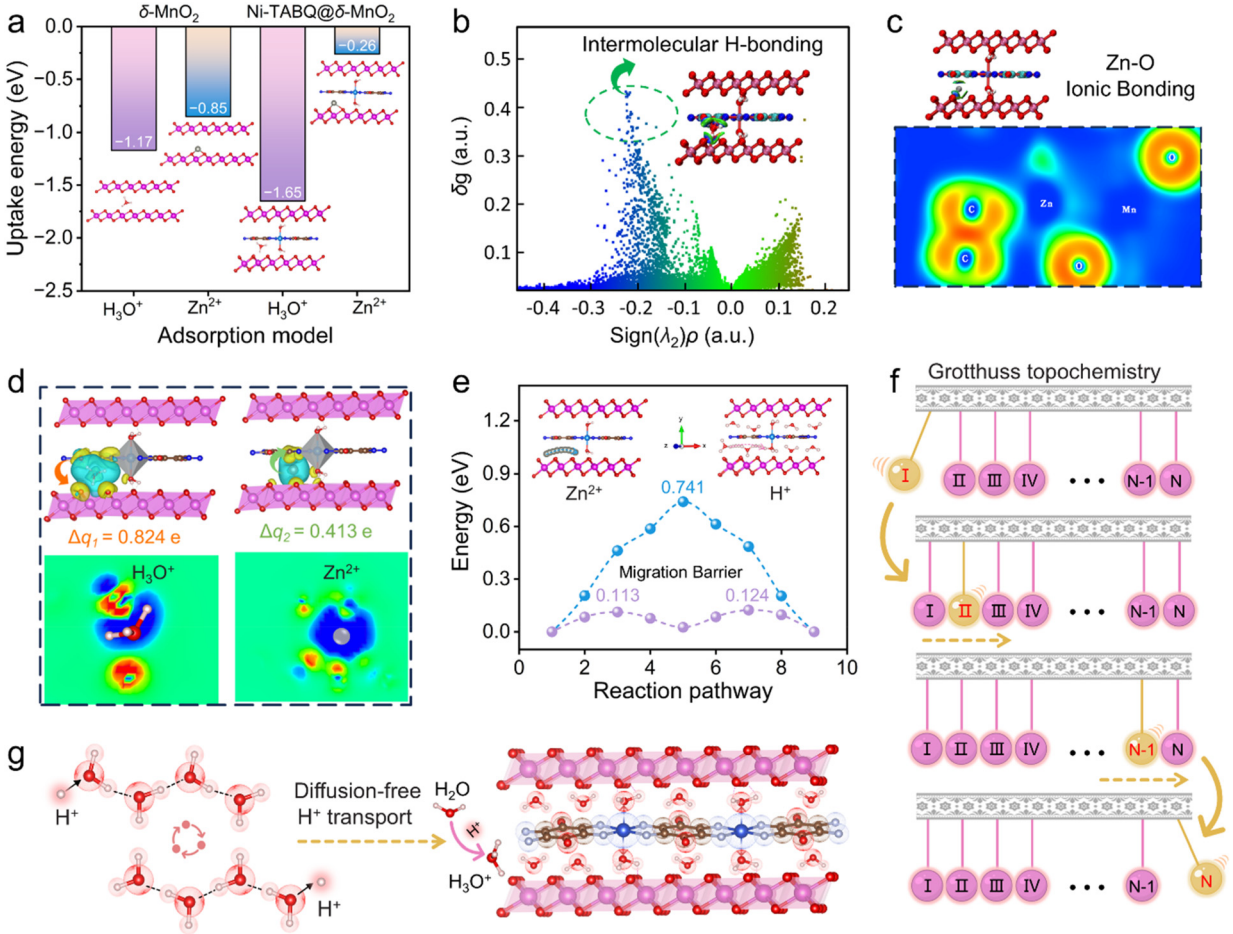

Fig. 5 Theoretical simulations of proton storage behaviors in the Ni–TABQ@δ-MnO_2 hybrid superlattice cathode. (a) The uptake energy of Zn^{2+} and H_3O^+ in the optimized crystal structure. (b) Plots of IGMH *versus* sign(λ_2)ρ and the corresponding gradient isosurfaces of H_3O^+ ions. (c) ELF maps of Zn^{2+} ions. (d) Differential charge isosurfaces and Bader charge transfer. (e) Migration energy barriers of Zn^{2+} and H^+ ions. (f) The Grotthuss topochemistry model of proton storage. (g) The diffusion-free H^+ transport mechanism in the hybrid superlattice Ni–TABQ@δ-MnO_2 cathode.

gen-bonding network primarily facilitates proton transport through the Grotthuss mechanism, which affords fast redox kinetics at Mn sites but does not directly influence Zn^{2+} migration. This ultra-low energy barrier for H^+ diffusion underscores the superior proton storage performance of the Ni–TABQ@δ-MnO_2 cathode.

Here, the Grotthuss proton transfer mechanism, also known as proton hopping, is demonstrated, representing an efficient and dynamic pathway for proton conduction in H-bonding systems (Fig. 5f). Unlike conventional Zn^{2+} ionic diffusion, where ions physically migrate across the host material, the Grotthuss mechanism relies on the rapid relay of protons through hydrogen-bonding networks. This process involves the transient breaking and reformation of H-bonds, allowing protons to "hop" between adjacent water molecules, contributing to diffusion-free H^+ transport (Fig. 5g). As a result, the net transport of protons occurs without the significant mass movement of ionic carriers, leading to faster proton mobility and reduced energy barriers. The strong protophilic nature of the hybrid superlattice TABQ@δ-MnO_2 framework plays a critical role in enabling Grotthuss topochemistry. The hydrated protons (H_3O^+) form dynamic and flexible H-bonds within Ni–TABQ@δ-MnO_2, creating an ideal environment for Grotthuss proton transfer. This well-connected H-bonding network facilitates the rapid and continuous hopping of protons, significantly enhancing the proton transport kinetics. Compared to rigid and slow Zn^{2+} transport through Zn–O ionic bonds, proton transfer *via* Grotthuss topochemistry ensures higher charge storage efficiency and faster response times during electrochemical reactions. Consequently, the Grotthuss mechanism contributes directly to the superior proton storage capabilities, high ionic conductivity, and enhanced energy storage performance of the Ni–TABQ@δ-MnO_2 cathode, making this a promising strategy for advanced energy storage systems.

Conclusions

We designed a hybrid superlattice Ni–TABQ@δ-MnO_2 cathode to enhance proton transfer through Grotthuss topochemistry, offering a promising solution for ultrahigh-rate Zn-ion batteries. By incorporating two-dimensional Ni–TABQ, the electronic properties of δ-MnO_2 are effectively modulated *via* π–d electron coupling, forming a highly efficient conductive network. The abundant intermolecular H-bonds between coordination water (Ni–TABQ) and lattice oxygen (δ-MnO_2) facilitate proton conduction with rapid redox reactions. Through the dynamic hopping of H_3O^+ ions, driven by the continuous breaking and reformation of O–H bonds within the intermolecular H-bonding network, Ni–TABQ@δ-MnO_2 achieves a significantly reduced charge transfer energy barrier (0.082 eV) compared to the sluggish Zn^{2+} diffusion process (0.741 eV). This fast-kinetics proton transport mechanism mitigates the lattice repulsion and phase instability associated with Zn^{2+} intercalation, ensuring a Ni–TABQ@δ-MnO_2 cathode with exceptional electrochemical metrics, including high capacity, excellent rate performance, and an ultralong lifespan. These findings underscore the importance of hybrid superlattice cathode structures with efficient proton transfer for advanced energy storage systems.

Data availability

The data that support the findings of this study are available on request from the corresponding author, upon reasonable request.

Conflicts of interest

The authors declare no conflicts of interest.

Acknowledgements

This work is financially supported by the National Natural Science Foundation of China (No. 22272118, 22172111 and 22309134), the Science and Technology Commission of Shanghai Municipality, China (No. 22ZR1464100, 20ZR1460300, and 19DZ2271500), China Postdoctoral Science Foundation (2022M712402), Shanghai Rising-Star Program (23YF1449200), Zhejiang Provincial Science and Technology Project (2022C01182), and the Fundamental Research Funds for the Central Universities (2023-3-YB-07).

References

1 Y. Dai, R. Lu, C. Zhang, J. Li, Y. Yuan, Y. Mao, C. Ye, Z. Cai, J. Zhu, J. Li, R. Yu, L. Cui, S. Zhao, Q. An, G. He, G. I. N. Waterhouse, P. R. Shearing, Y. Ren, J. Lu, K. Amine, Z. Wang and L. Mai, *Nat. Catal.*, 2024, **7**, 776–784.
2 S. Li and C. Zhi, *Adv. Mater.*, 2024, **36**, 2413515.
3 X. Yu, M. Chen, Z. Li, X. Tan, H. Zhang, J. Wang, Y. Tang, J. Xu, W. Yin, Y. Yang, D. Chao, F. Wang, Y. Zou, G. Feng, Y. Qiao, H. Zhou and S.-G. Sun, *J. Am. Chem. Soc.*, 2024, **146**, 17103–17113.
4 X. Zhang, J. Li, Y. Liu, B. Lu, S. Liang and J. Zhou, *Nat. Commun.*, 2024, **15**, 2735.
5 X. Shi, J. Zeng, A. Yi, F. Wang, X. Liu and X. Lu, *J. Am. Chem. Soc.*, 2024, **146**, 20508–20517.
6 D. Chao, R. DeBlock, C.-H. Lai, Q. Wei, B. Dunn and H. J. Fan, *Adv. Mater.*, 2021, **33**, 2103736.
7 Y. Ding, C. Cai, L. Ma, J. Wang, M. P. Mercer, J. Liu, D. Kramer, X. Yu, D. Xue, C. Zhi and C. Peng, *Adv. Energy Mater.*, 2024, **14**, 2402819.
8 J. Yang, S. Bi, H. Wang, Y. Zhang, H. Yan and Z. Niu, *Angew. Chem., Int. Ed.*, 2024, **63**, e202409071.
9 F. Ye, Q. Liu, C. Lu, F. Meng, T. Lin, H. Dong, L. Gu, Y. Wu, Z. Tang and L. Hu, *Energy Storage Mater.*, 2022, **52**, 675–684.

10 Q. Wang, W. Zhou, Y. Zhang, H. Jin, X. Li, T. Zhang, B. Wang, R. Zhao, J. Zhang, W. Li, Y. Qiao, C. Jia, D. Zhao and D. Chao, *Natl. Sci. Rev.*, 2024, **11**, nwae230.
11 Y. Liu, L. Lin, T. Zhang, Z. Xue, J. Liu, D. Chao and X. Sun, *Energy Environ. Sci.*, 2024, **17**, 2521–2529.
12 Y. Liu, X. Cui, Y. Cao, G. Li, J. Chen and Y. Wang, *ACS Energy Lett.*, 2023, **8**, 3639–3645.
13 Z. Liu, M. Qin, B. Fu, M. Li, S. Liang and G. Fang, *Angew. Chem., Int. Ed.*, 2024, **63**, e202417049.
14 Y. Jin, L. Zou, L. Liu, M. H. Engelhard, R. L. Patel, Z. Nie, K. S. Han, Y. Shao, C. Wang, J. Zhu, H. Pan and J. Liu, *Adv. Mater.*, 2019, **31**, 1900567.
15 S. Bi, Y. Zhang, S. Deng, Z. Tie and Z. Niu, *Angew. Chem., Int. Ed.*, 2022, **61**, e202200809.
16 H. Lin, L. Zeng, C. Lin, J. Wu, H. He, C. Huang, W. Lai, P. Xiong, F. Xiao, Q. Qian, Q. Chen and J. Lu, *Energy Environ. Sci.*, 2025, **18**, 1282–1293.
17 K. Zhou, G. Liu, X. Zhu, G. Liu, X. Yu, Z. Guo and Y. Wang, *Angew. Chem., Int. Ed.*, 2024, **63**, e202413959.
18 D. Xu, D. Zheng, F. Wang, X. Shang, Y. Wang and X. Lu, *Energy Environ. Sci.*, 2024, **17**, 8094–8101.
19 Y. Zhao, R. Zhou, Z. Song, X. Zhang, T. Zhang, A. Zhou, F. Wu, R. Chen and L. Li, *Angew. Chem., Int. Ed.*, 2022, **61**, e202212231.
20 Y. Chen, L. Miao, Z. Song, H. Duan, Y. Lv, L. Gan and M. Liu, *Adv. Funct. Mater.*, 2024, **34**, 2409428.
21 D. Bin, W. Huo, Y. Yuan, J. Huang, Y. Liu, Y. Zhang, F. Dong, Y. Wang and Y. Xia, *Chem*, 2020, **6**, 968–984.
22 X. Liu, Y. Yao, D. Wang, S. Yao, S. Wang, Z. Fu, Y. Li, J. Wang, Z. Hou, X. Gao, Z. Yang and Y. M. Yan, *Adv. Energy Mater.*, 2023, **13**, 2300384.
23 W. Sun, F. Wang, S. Hou, C. Yang, X. Fan, Z. Ma, T. Gao, F. Han, R. Hu, M. Zhu and C. Wang, *J. Am. Chem. Soc.*, 2017, **139**, 9775–9778.
24 J. Zhang, W. Li, J. Wang, X. Pu, G. Zhang, S. Wang, N. Wang and X. Li, *Angew. Chem., Int. Ed.*, 2023, **62**, e202215654.
25 A. Zhang, R. Zhao, Y. Wang, J. Yue, J. Yang, X. Wang, C. Wu and Y. Bai, *Angew. Chem., Int. Ed.*, 2023, **62**, e202313163.
26 Q. Chen, X. Lou, Y. Yuan, K. You, C. Li, C. Jiang, Y. Zeng, S. Zhou, J. Zhang, G. Hou, J. Lu and Y. Tang, *Adv. Mater.*, 2023, **35**, 2306294.
27 Z. Chen, Z. Huang, C. Wang, D. Li, Q. Xiong, Y. Wang, Y. Hou, Y. Wang, A. Chen, H. He and C. Zhi, *Angew. Chem., Int. Ed.*, 2024, **63**, e202406683.
28 Y. Liang, H. Zhang, M. Huo, X. Zhang, K. Qin, H. Wang, Q. Li, X. Zhao, Z. Xing, J. Chang and G. Zhu, *Adv. Mater.*, 2024, **36**, 2415545.
29 X. Shi, J. Xie, J. Wang, S. Xie, Z. Yang and X. Lu, *Nat. Commun.*, 2024, **15**, 302.
30 Z. Yu, Q. Wang, Y. Li, F. Zhang, X. Ma, X. Zhang, Y. Wang, J. Huang and Y. Xia, *Joule*, 2024, **8**, 1063–1079.
31 Q. Zhao, A. Song, W. Zhao, R. Qin, S. Ding, X. Chen, Y. Song, L. Yang, H. Lin, S. Li and F. Pan, *Angew. Chem., Int. Ed.*, 2021, **60**, 4169–4174.
32 F. Zhao, J. Li, A. Chutia, L. Liu, L. Kang, F. Lai, H. Dong, X. Gao, Y. Tan, T. Liu, I. P. Parkin and G. He, *Energy Environ. Sci.*, 2024, **17**, 1497–1508.
33 Q. Zhao, A. Song, S. Ding, R. Qin, Y. Cui, S. Li and F. Pan, *Adv. Mater.*, 2020, **32**, 2002450.
34 L. Wang, Y. Ni, X. Hou, L. Chen, F. Li and J. Chen, *Angew. Chem., Int. Ed.*, 2020, **59**, 22126–22131.
35 H. Yang, W. Zhou, D. Chen, J. Liu, Z. Yuan, M. Lu, L. Shen, V. Shulga, W. Han and D. Chao, *Energy Environ. Sci.*, 2022, **15**, 1106.
36 Z. Song, L. Miao, Y. Lv, L. Gan and M. Liu, *Angew. Chem., Int. Ed.*, 2023, **62**, e202309446.
37 Y. Zhang, Z. Song, L. Miao, Y. Lv, L. Gan and M. Liu, *Angew. Chem., Int. Ed.*, 2024, **63**, e202316835.
38 T. Lu and Q. Chen, *J. Comput. Chem.*, 2022, **43**, 539–555.
39 S. Zhu, R. Yang, H. J. W. Li, S. Huang, H. Wang, Y. Liu, H. Li and T. Zhai, *Angew. Chem., Int. Ed.*, 2024, **63**, e202319462.
40 S. Zheng, X. Yang, Z.-Z. Shi, H. Ding, F. Pan and J.-F. Li, *J. Am. Chem. Soc.*, 2024, **146**, 26965–26974.
41 P.-C. Shen, C. Su, Y. Lin, A.-S. Chou, C.-C. Cheng, J.-H. Park, M.-H. Chiu, A.-Y. Lu, H.-L. Tang, M. M. Tavakoli, G. Pitner, X. Ji, Z. Cai, N. Mao, J. Wang, V. Tung, J. Li, J. Bokor, A. Zettl, C.-I. Wu, T. Palacios, L.-J. Li and J. Kong, *Nature*, 2021, **593**, 211–217.
42 L. Cui, S. Zhang, J. Ju, T. Liu, Y. Zheng, J. Xu, Y. Wang, J. Li, J. Zhao, J. Ma, J. Wang, G. Xu, T.-S. Chan, Y.-C. Huang, S.-C. Haw, J.-M. Chen, Z. Hu and G. Cui, *Nat. Energy*, 2024, **9**, 1084–1094.
43 H. Lu, Q. Zeng, L. Xu, Y. Xiao, L. Xie, J. Yang, J. Rong, J. Weng, C. Zheng, Q. Zhang and S. Huang, *Angew. Chem., Int. Ed.*, 2024, **63**, e202318859.
44 S. Zhao, L. Yin, L. Deng, J. Song, Y.-M. Chang, F. Hu, H. Wang, H.-Y. Chen, L. Li and S. Peng, *Adv. Funct. Mater.*, 2023, **33**, 2211576.
45 Z. Song, L. Miao, L. Ruhlmann, Y. Lv, D. Zhu, L. Li, L. Gan and M. Liu, *Adv. Mater.*, 2021, **33**, 2104148.
46 Z. Song, L. Miao, H. Duan, Y. Lv, L. Gan and M. Liu, *Angew. Chem., Int. Ed.*, 2024, **63**, e202401049.
47 X. Li, D. He, Q. Zhou, X. Zhou, Z. Wang, C. Wei, Y. Shi, X. Hu, B. Huang, Z. Yang, X. Han, Y. Lin and Y. Yu, *Energy Environ. Sci.*, 2024, **17**, 9195–9204.
48 T. Wang, J. Jin, X. Zhao, X. Qu, L. Jiao and Y. Liu, *Angew. Chem., Int. Ed.*, 2024, **63**, e202412057.
49 N. Jiang, Y. Zeng, Q. Yang, P. Lu, K. Qu, L. Ye, X. Lu, Z. Liu, X. Li, Y. Tang, J. Cao, S. Chen, C. Zhi and J. Qiu, *Energy Environ. Sci.*, 2024, **17**, 8904–8914.
50 Y. Wang, S. Wei, Z.-H. Qi, S. Chen, K. Zhu, H. Ding, Y. Cao, Q. Zhou, C. Wang, P. Zhang, X. Guo, X. Yang, X. Wu and L. Song, *Proc. Natl. Acad. Sci. U. S. A.*, 2023, **120**, e2217208120.
51 H. Geng, M. Cheng, B. Wang, Y. Yang, Y. Zhang and C. C. Li, *Adv. Funct. Mater.*, 2020, **30**, 1907684.
52 S. Liu, H. Zhu, B. Zhang, G. Li, H. Zhu, Y. Ren, H. Geng, Y. Yang, Q. Liu and C. C. Li, *Adv. Mater.*, 2020, **32**, 2001113.

53 H. Lu, S. Meng, T. He, C. Zhang and J. Yang, *Coord. Chem. Rev.*, 2024, **514**, 215910.
54 C. Ding, Y. Wang, C. Li, J. Wang, Q. Zhang and W. Huang, *Chem. Sci.*, 2024, **15**, 4952–4959.
55 Z. Song, L. Miao, L. Ruhlmann, Y. Lv, L. Gan and M. Liu, *Angew. Chem., Int. Ed.*, 2023, **62**, e202219136.
56 W. Lyu, H. Fu, A. M. Rao, Z. Lu, X. Yu, Y. Lin, J. Zhou and B. Lu, *Sci. Adv.*, 2024, **10**, eadr9602.
57 J.-J. Ye, P.-H. Li, Z. Hou, W. Zhang, W. Zhu, S. Jin and H. Ji, *Angew. Chem., Int. Ed.*, 2024, **63**, e202410900.
58 H. Zhang, W. Wu, Q. Liu, F. Yang, X. Shi, X. Liu, M. Yu and X. Lu, *Angew. Chem., Int. Ed.*, 2021, **60**, 896–903.